Highly Crystalline Colloidal Nickel Oxide Hole Transport Layer for Low Temperature Processable Perovskite Solar Cell

Pei-Huan Lee,[1] Ting-Tzu Wu,[1] Chia-Feng Li,[2] Damian Głowienka,[1,3] Yi-Hsuan Sun,[1] Yi-Ting Lin,[1] Hung-Wei Yen,[1] Cheng-Gang Huang,[1] Yulia Galagan,[1] Yu-Ching Huang[2]* and Wei-Fang Su[1]*

1Dept. of Materials Science and Engineering, National Taiwan University, Taipei, Taiwan

2Dept. of Materials Engineering, Ming Chi University of Technology, New Taipei, Taiwan

3Faculty of Applied Physics and Mathematics, Gdańsk University of Technology, Gdańsk, Poland

E-mail: huangyc@mail.mcut.edu.tw; suwf@ntu.edu.tw

Abstract

Highly crystalline NiO_X usually requires high annealing temperature (>300 °C) which is incompatible with flexible substrate and might consume high amount of energy. Herein, we demonstrate a facile emulsion process to synthesize highly crystalline, low temperature (> 150 °C) and solution processable NiO_x nanoparticles (NPs) as a hole transport layer for the perovskite solar cells (PVSCs). A novel surfactant of tetramethylammonium hydroxide (TMAOH) was used to react with $Ni(NO_3)_2$ to form $Ni(OH)_2$ nanoparticles (NPs). The micelles of TMAOH act as a nano-reactor containing OH^- anion. The Ni^+ cation enters into the nano-reactor to form $Ni(OH)_2$ NPs inside the reactor with controlled particle size. The $Ni(OH)_2$ NPs prepared by emulsion process and chemical precipitation method are further calcined to form NiO_X NPs with the particle size of 8.28±2.64 nm (EP-NiO_X). The smaller size of EP-NiO_X NPs results in a good dispersibility and an excellent stability of NPs suspension, which can be used to fabricate uniform NiO_X film without any aggregates. A power conversion efficiency (PCE) of 18.85% can be achieved using this EP-NiO_X film, as compared with 16.68% using the NiO_X NPs synthesized from the chemical precipitation method (CPM-NiO_X). Moreover, a flexible PVSCs with a PCE of 14.28% can be fabricated using the EP-NiO_X film. Except for the device performance, the quality of the EP-NiO_X film shows a good batch-to-batch uniformity, resulting in an excellent reproducibility of PVSCs. This work has a potential for the development of a large-scale production of PVSCs with a high energy conservation.

Keywords: emulsion process, nickel oxide, hole transport layer, low temperature, perovskite solar cell

1. Introduction

Organic-inorganic metal halide perovskites solar cells (PVSCs) have attracted enormous attention because of their high power conversion efficiency (PCE). Recently, the highest certified PCE of 25.2% has been reported.[1] Several architectures of PVSCs have been developed over these years. Among them, the conventional n-i-p structure[2-4] and inverted p-i-n structure[4, 5] are the most common device structures. For the inverted p-i-n structure, the PVSCs have the structure of glass/bottom electrode/hole transporting layer (HTL)/perovskite layer/electron transporting layer (ETL)/top electrode. The functions of the HTL and ETL are to extract hole and electron carriers, respectively. Also tehri role is to prevent the recombination of photo-generated carriers. To date, many p-type semiconductors, such as PEDOT:PSS,[6,7] PTAA,[5,8] CuSCN,[9] CuO_X[10] and NiO_X[11,12] have been utilized as HTL. Although, organic p-type semiconductors can be processed at low temperature (< 150 ºC), but they have poor long-term stability. To overcome this limitation, thermal and chemical stable inorganic p-type semiconductors have been widely used as the HTL. Among them, NiO_X is very attractive for the p-i-n PVSCs due to the advantages of outstanding stability, low cost, and deep valence band.[13] Recently, many efficient and stable PVSCs were fabricated using NiO_X HTL.[14, 15]

Many techniques have been used to fabricate NiO_X thin films, including solution process,[11,14] sputtering[16-18] and atomic layer deposition.[19] Among them, the solution process draws a special attention due to its low manufacturing cost and the feasibility for large scale process. At present, sol-gel process is the most common technique for fabricating NiO_X film, but it requires high reaction temperature (> 300 ºC) and long heating time (> 30 min) to have highly crystalline film.[20,21] The process not only limits the application for flexible PVSCs, but also has high manufacturing cost with a high energy consumption. From the commercialization point of view, the low-temperature solution processable NiO_X is highly desired; consequently, NiO_X nanoparticles (NPs) suspension has been extensively studied to meet the goal. For the NiO_X NPs suspension, the NiO_X NPs have to be highly crystalline and well dispersed in the solvent to obtain the high quality film, thus a device with high performance can be achieved.

Liang et al. introduced a lithium stearate to bind on the surface of NiO$_X$ NPs during the synthesis process.[22] The uniform-sized NiO$_X$ NPs can be well dispersed in chloroform. Liu et al. used the similar procedure to prepare NiO$_X$ NPs ink and used this ink to prepare NiO$_X$ film at 150°C.[23] The PVSCs fabricated using this NiO$_X$ film perform a PCE of 15.9%. However, the long alkyl chain of stearate is an insulator, which limits the performance of PVSCs. Yin, et al. used chemical precipitation method (CPM) to prepare NiO$_X$ NPs first by reacting nickel nitrate with sodium hydroxide to form nickel hydroxide (Ni(OH)$_2$), then through the calcination to form NiO$_X$ NPs. This NiO$_X$ NPs can be dispersed in deionized water and formed film at low temperature of 150 °C. The PCE of PVSCs fabricated using this NiO$_X$ HTL can reach to 16.47%.[24] Zhang, et al. applied this NiO$_X$ film to PVSCs and obtain the PCE of rigid and flexible PVSCs being 17.6% and 14.6%, respectively.[25] Nevertheless, we found that NiO$_X$ NPs synthesized from CPM is difficult to reproduce the size distribution and dispersibility because the precise control of the pH, titration rate and reaction temperature is required in every batch. Thus, the high reproducibility of performance of PVSCs fabricated from CPM-NiO$_X$ NPs cannot be obtained.

Here we report an emulsion process (EP) [26] to synthesize NiO$_X$ NPs with controlled size and distribution with consistent quality from batch-to-batch. A novel surfactant of tetramethyl ammonium hydroxide (TMAOH) was used to react with nickel nitrate to form Ni(OH)$_2$ colloidal particles. The micelles of TMAOH act as nano-reactor containing OH$^-$ anion. The Ni$^+$ cation enters into the reactor to form Ni(OH)$_2$ inside the reactor with controlled particle size and distribution. The Ni(OH)$_2$ NPs prepared by the emulsion process and the chemical precipitation method are further calcined to form NiO$_X$ NPs with the particle size equal to 8.28±2.64 nm (EP-NiO$_X$) and 15.12±6.32 nm (CPM-NiO$_X$), respectively. The smaller size of EP-NiO$_X$ NPs results in good a dispersibility and excellent stability of NPs suspension. Therefore, the uniform and smooth EP-NiO$_X$ film with a good interfacial contact with the perovskite film can be obtained, which leads to an enhanced PCE of 18.85% compared to 16.68% of PVSCs fabricated from CPM-NiO$_X$. To the best of our knowledge, the 18.85% PCE is the highest reported value for the PVSCs fabricated from the low temperature (< 150 °C) and solution processable pristine NiO$_X$ NPs. State-of-the-art NiO$_X$ NPs based p-i-n PVSCs are shown in **Table S1**. The flexible PVSCs were also fabricated from the EP-NiO$_X$ film with a PCE of 14.3%. In addition to the improvement of device performance, the consistent device performance is also achieved due to the highly

reproducible film quality of EP-NiO$_X$ NPs using different batches of NPs. The HTL film of EP-NiO$_X$ NPs developed in this work has the potential for a low temperature, solution processable process to fabricate a large scale highly efficient PVSCs with the advantageous of low cost and a low energy consumption.

2. Experimental Method

2.1 Materials

Chlorobenzene (CB, >99.0%), *N,N*-dimethylformamide (DMF , 99.8%,), dimethyl sulfoxide (DMSO, >99.9%) and isopropyl alcohol (IPA, 99.8%) were pruchased from Acros Organics. Tetramethylammonium hydroxide pentahydrate (TMAOH, ≥97%) and sodium hydroxide (NaOH) have been pruchased from Sigma Aldrich. Diethyl ether (99.0%) and ethanol (99.99%) were pruchased from Fisher Chemical. Acetone (99.0%), polyethylenimine (PEI, branched, M$_W$ ~25000), nickel nitrate hexahydrate (Ni(NO$_3$)$_2$ · 6H$_2$O, 98%) have been purchased from Alfa Aesar. Fluorine-doped tin oxide (FTO) glasses, methylammonium iodide (MAI), lead iodide (PbI$_2$, 99.9985%) and [6,6]-phenyl-C$_{61}$-butyric acid methyl ester (PC$_{61}$BM, 99.0%) were purchased from FrontMaterials Co. Ltd.

2.2. Synthesis of NiO$_X$ nanoparticles and preparation of NiO$_X$ suspensions

5 M Ni(NO$_3$)$_2$ · 6H$_2$O was dissolved in deionized water to obtain a clear green solution. For the chemical precipitation method, the pH value of the nickel nitrate solution was adjusted to 10 by adding a 10 M NaOH. For the emulsion process, the 10 M NaOH aqueous solution was replaced by 10 M TMAOH aqueous solution. After adding NaOH or TMAOH aqueous solution, the green product of Ni(OH)$_2$ nanoparticles (NPs) have been precipitated out. The Ni(OH)$_2$ NPs were then washed by deionized for five times, collected by centrifugation, and dried at 80°C overnight. The dried Ni(OH)$_2$ powder was calcined at 270°C for 2 h to obtain dark NiO$_X$ NPs powder. Note that the NiO$_X$ NPs synsesized from the chemical precipitation method and the emulsion process is denoted as CPM-NiO$_X$ and EP-NiO$_X$, respectively. Finally, the CPM-NiO$_X$ or EP-NiO$_X$ were dispersed in deionized water with a concentration of 15 mg/mL.

2.3. Fabrication of rigid perovskite solar cells

FTO glass was washed with acetone, methanol and isopropanol sequentially, followed by O$_2$ plasma treatment for 15 min. The EP-NiO$_X$ or CPM-NiO$_X$ suspension was then spin-coated onto cleaned FTO glass

4

at 2500 rpm for 60 s, followed by annealing at 150°C for 20 min in air to remove remaining water. The perovskite precursor solution was prepared by mixing 552 mg of PbI_2 and 190.8 mg of MAI in 1 mL mixed solvent of DMF and DMSO (5:2, v/v). Subsequently, the perovskite precursor was then spin-coated onto the NiO_X films at 4500 rpm for 30 s in the glove box. 15 s before the end of the spinning process, a 300 μL of diethyl ether was dropped onto the perovskite film. Then, the samples were sequentially annealed on the hot-plate at 60°C for 1 min and 100°C for another 2 min to form dark-brown perovskite film. After cooling to the room temperature, the $PC_{61}BM$ solution (2.5 wt.% in chlorobenzene) was spin-coated onto the perovskite layer at 1000 rpm for 30 s to serve as the ETL. Then, the work function modifier of PEI (0.1 wt% in IPA) was spin-coated onto the $PC_{61}BM$ layer at 3000 rpm for 30 s without further annealing. Finally, the samples were transferred to a chamber and the Ag electrodes with 100 nm thickness were thermally evaporated on the top of PCBM/PEI under a high vacuum ($<5 \times 10^{-6}$ torr).

2.4 Fabrication of flexible perovskite solar cells

The mica/AZO-ITO substrate was supplied by Prof. Ying-Hao Chu of National Chiao Tung University, Taiwan. The clean process of mica/AZO-ITO, the depositions of TMAOH-NiO_X suspension, perovskite, PCBM, PEI and Ag were the same as rigid PVSCs.

2.5 Characterization

The J-V curves of devices with 0.09 cm^2 active area were measured from both forward (from −0.2 to 1.2 V) and backward (from 1.2 to −0.2 V) scans. The step voltage of the test and the delay time was 50 mV and 10 ms, respectively. The measurement has been done by a voltage source meter (Keithley 2410) under an AM 1.5G solar simulator (Yamashita Denso) with an irradiation of 100 mW/cm^2. Also, a set of filters have been used to obtain 100, 80, 52, 27, 12 and 3 $mW\ cm^{-2}$ light illumination intensities. All the devices were measured in air. Transmission electron microscopy (TEM) images of EP-NiO_X and CPM-NiO_X NPs were obtained from a FEI transmission electron microscope (JEOL JEM-2100). The crystal structure of EP-NiO_X and CPM-NiO_X was determined by an X-ray diffractometer (XRD, Malvern Panalytical, X'Pert PRO MPD). The work function of EP-NiO_X and CPM-NiO_X films was measured by ultraviolet photoelectron spectroscopy (PHI 5000 VersaProbe, ULVAC-PHI) using ultraviolet light source of He I emission (21.2 eV, B50 W) and

calculated by the equation of $\Phi = h\nu - (E_0 - E_F)$. The X-ray photoelectron spectroscopy (XPS) spectra were recorded with a PHI 5000 Versa Probe system (ULVAC-PHI, Chigasaki) using a micro focused (100 μm, 25 W) Al X-ray beam. The surface morphology and roughness of EP-NiO$_X$ and CPM-NiO$_X$ films have been measured by atomic force microscopy (AFM, PARK XE-70). The size distribution and the zeta potential of EP-Ni(OH)$_2$ and CPM-Ni(OH)$_2$ NPs in DI water were measured by dynamic light scattering (DLS, HORIBA SZ-100). The thermal property of TMAOH surfactant, EP-NiO$_X$ and CPM-NiO$_X$ was analyzed by thermal gravimetric analysis (TGA, TAInstrument Q50) in air at a heating rate of 5^oC/min. Specimens for cross-sectional observations were prepared by a dual-beam focused ion beam (FIB) system (Helios Nanolab 600i, FEI, Oregon, USA) equipped with through lens detector (TLD). The top surface of a specimen was initially deposited with a 30 nm-thick carbon layer by electron beam at an accelerating voltage of 1 kV and a probe current of 86 pA. Subsequently, the other 1 μm thick carbon layer was deposited by ion beam at an accelerating voltage of 30 kV and a probe current of 40 pA. In the lift-out process, a probe current of 2.5 nA under 30 kV was used for the regular cross sectioning and U-shaped cutting. A probe current of lower than 1 nA under 30 kV was used for all cleaning processes. Moreover, to minimize the beam damage on materials, a probe current of 39 pA under 2 kV was applied in the final trimming into the thin foil. An elemental mapping of X-ray energy-dispersive spectrum (EDS) was done before the final trimming. Signals of X-ray EDS were collected by Ultim Extreme detector, manufactured by Oxford Instruments. Ultim Extreme detector delivers up to extremely high sensitivity than a conventional silicon drift detector, and, therefore, low-energy X-rays, i.e. M-series or L-series, can be effectively collected and processed. This enables application of lower acceleration voltage and lower electron dose during collection of characteristic X-rays, leading to higher spatial resolution and lower beam damage. In this work, X-ray EDS mapping was conducted at an accelerating voltage of 5 kV and a probe current of 690 pA under immersion mode. The photoluminescence (PL) spectra were recorded with a continuous-wave diode laser source (PDLH-440-25, DongWoo Optron Co. Ltd.), and the emission spectra were recorded with a photomultiplier tube detector system (PDS-1, DongWoo Optron Co. Ltd.). The time-resolved photoluminescence (TRPL) spectra have been recorded using a time correlated single photon counting spectrometer (WELLS-001, FX, DongWoo Optron Co.Ltd.). The pulse laser had a wavelength of 440 nm and an average power of 1 mW was operated with excitation duration of 2 μs. To figure out the trap-

density of perovskite fabricated on EP-NiO$_X$ and CPM-NiO$_X$ films, the devices with hole-only device structure of FTO/EP-NiO$_x$ or CPM-NiO$_X$/perovskite/Au were fabricated. The measurement was carried out with the applied voltage ranging from 0 to 5 V.

3. Results and Discussion

To prepare the low temperature, solution processable and high quality NiOx HTL, one has to synthesize highly crystalline and highly dispersible nickel oxide nanoparticles. In general, a high dispersion stability is important for the processing of nanoparticle dispersion. However, the nanoparticles are usually attracted by each other to form aggregates because of the Van-der-Waals interaction, which affect the dispersibility of nanoparticles and stability of nanoparticle dispersion. Therefore, the repulsive force among the particles against aggregation is required. We employed two different synthetic approaches, the emulsion process (**Figure 1(a)**) and the chemical precipitation method (**Figure 1(b)**) to firstly prepare nickel hydroxide (Ni(OH)$_2$) NPs. Then the Ni(OH)$_2$ NPs were calcined into NiO$_X$ NPs at 270 ^{o}C.. We carefully investigated the characteristics of two kinds of NPs in solution and in the film. For the emulsion process,[26] we reacted nickel nitrate aqueous solution with a micelle solution of surfactant containing hydroxide anion to avoid the aggregation. Generally, the selection principle of surfactant for emulsion process include: (1) the surfactant should be high basicity to provide hydroxide anion; (2) the surfactant should possess an organic part to form micelles; (3) the surfactant should exhibit low decomposition temperature to ensure that it can be completely removed after calcination. Following this principle, the tetramethylammonium hydroxide (TMAOH) can form the micelles, which act as nano-reactor containing hydroxide anions, for the synthesis of Ni(OH)$_2$ NPs. The

7

formation of micelles nano-reactor was evidenced by dynamic light scattering (DLS) measurement as shown in **Figure S1**. Moreover, the decomposition temperature (~150 °C) of TMAOH is much lower than the calcination temperature of NiOx (270 °C), as shown in thermal gravimetric analysis (TGA) of TMAOH (**Figure S2**).[27] The low decomposition temperature of TMAOH ensures that the TMAOH can be completely removed after calcination. Therefore, we have chosen TMAOH as the surfactant for the emulsion process. Upon in contacting with the nickel nitrate solution, the nickel cations enter into the micelles of TMAOH to form EP-Ni(OH)$_2$ nanoparticles suspension as shown in **Figure 1(a)**. The solution is stable after one-day storage. For the chemical precipitation method, the NaOH aqueous solution was added to react with nickel nitrate solution. The CPM-Ni(OH)$_2$ NPs were precipitated out after the reaction but the dispersion of CPM-Ni(OH)$_2$ was not stable after one-day storage, as shown in **Figure 1(b)**. To prove the formation of EP-Ni(OH)$_2$ was taken place in the micelle, the DLS and zeta potential measurement were conducted. The DLS measurements of suspensions (**Figure 1(c)** and **Figure 1(d)**) show that the mean particle size of aggregated nanoparticles of EP-Ni(OH)$_2$ is approximately to two order smaller than that of CPM-Ni(OH)$_2$ (77.30 nm versus 5945 nm). The huge difference between EP-Ni(OH)$_2$ and CPM-Ni(OH)$_2$ originates from the formation of TMAOH micelles in the Ni(NO$_3$)$_2$ aqueous solution. The reaction takes place in the micelles to generate EP-Ni(OH)$_2$ nanoparticles, which prevents the EP-Ni(OH)$_2$ NPs from the aggregation. In the contrast, the CPM-Ni(OH)$_2$ aggregates are too large to be suspended in the solution. We also measured the zeta potential of aggregates of EP-Ni(OH)$_2$ NPs and CPM-Ni(OH)$_2$ in DI water with the values of 40.78 mV and 4.67 mV, respectively (**Figure S3**). The positive charge of TMA cations remained on the surface of Ni(OH)$_2$ and kept the aggregates floating in the solution. On the other hand, there is no micelles formation in the CPM process,

8

the sodium cations do not surround around the aggregates but stay in the solution that results in low zeta potential of 4.67 mV.

The NiO_X NPs were indeed obtained from both approaches after calcination of $Ni(OH)_2$ at 270 °C for 2 h, which was proved through the investigations of transmission electron microscopy (TEM) and X-ray diffraction measurement (XRD). **Figure 2(a)** and **2(b)** shows the TEM images of CPM-NiOx NPs and EP-NiOx NPs, respectively. From the TEM images, we can clearly observe a large aggregate and a random shaped $CPM-NiO_X$ NPs with an average diameter of 15.12 nm and a distribution of particles size from 6 to 45 nm (**Figure 2(c)**). It is worth noting that the large aggregate has been formed since the synthesis process of CPM-$Ni(OH)_2$ NPs. On the other hand, the $EP-NiO_X$ NPs exhibit a spherical shape with a narrow size distribution and an average diameter equal to 8.28 nm (**Figure 2(d)**). The smaller size and narrower size distribution of $EP-NiO_X$ is contributed by the reaction that occurred within a micelle. From the selected area electron diffraction (SAED) patterns (**Figure 2(e)** and **(f)**), we can find both SAED patterns that show three rings, whereas (111), (220) and (200) represents crystal planes of rock salt NiO_x, respectively. There are no impurity phases in both NiOx NPs. These results are consistent with the XRD measurement, and the related XRD patterns are shown in **Figure S4**. To prove the TMAOH were completely removed after calcination, we conducted TGA analysis of EP-NiOx and CPM-NiOx as shown in **Figure S5**. The two thermogram curves are very similar which indicates that there is no residual TMAOH on the surface of $EP-NiO_X$. We further characterize the chemical composition and work function of the $CPM-NiO_X$ and $EP-NiO_X$ NPs by X-ray photoelectron spectroscopy (XPS) and ultraviolet photo-electron spectroscopy (UPS) measurements. **Figure S6(a)** depicts the XPS Ni $2p_{3/2}$ spectra for $CPM-NiO_X$ and $EP-NiO_X$ NPs respectively. There are three peaks located at 853, 854.9, and 860.0 eV corresponding to Ni^{2+}, Ni^{3+}, and shake-up satellites. The $CPM-NiO_X$ and $EP-NiO_X$ films show the similar Ni^{3+}/Ni^{2+} ratio of 1.37 and 1.43, respectively. In addition to Ni spectrum, **Figure S6(b)** presents the XPS O 1s pattern consisting of three peaks located at 528.43, 530.14, and 531.76 eV, indicating to lattice oxygen, oxygen vacancy, and NiOOH, respectively. Both $CPM-NiO_X$ and $EP-NiO_X$ NPs show the same peak positions of the Ni $2p_{3/2}$ and O 1s patterns, which means that the EP-NiOx NPs exhibit the same chemical composition as $CPM-NiO_X$ NPs. The work function values of $CPM-NiO_X$ and EP-

NiO$_X$ were calculated from the UPS spectrum, as shown in **Figure S7**. The work function of EP-NiO$_X$ NPs is equal to –5.0 eV, which is the same as for CPM-NiO$_X$ NPs. Moreover, the devices with a configuration of FTO/CPM-NiO$_X$/Au or FTO/EP–NiO$_X$/Au were fabricated to measure the conductivity of each layer. The results have shown the same conductivity for both NiO$_X$ films (**Figure S8**). According to these results, we can demonstrate that the EP-NiOx NPs exhibit similar crystal structure, chemical composition, work function and conductivity to CPM-NiOx NPs. To prepare the NiO$_X$ NPs suspension, the obtained NiO$_X$ NPs were dispersed in DI water. Then, we left the CPM-NiO$_X$ and EP-NiO$_X$ aqueous solutions stand for 1 month to investigate the colloidal stability of these two solutions. As shown in **Figure 2(g)**, an obvious sedimentation can be observed from the CPM-NiO$_X$ suspension after standing for one month, while the EP-NiO$_X$ suspension remains dark without any changes. Although, after the calcination, both EP-NiO$_X$ and CPM-NiO$_X$ can be stabilized in DI water by electrostatic repulsive force, which is proved by zeta potential measurement of EP-NiO$_X$ and CPM-NiO$_X$ with the values of 44.31 mV and 40.72 mV (**Figure S9**), respectively. The gravitational force also affects the stability of nanoparticles dispersion and the sedimentation is slower for EP-NiO$_X$ dispersion due to the smaller particle size and absence of large aggregate, compared to CPM-NiO$_X$ dispersion. At sufficiently small particle sizes, rapid diffusion compensates for gravity and prevents particles from settling [ref]. Therefore, the EP-NiO$_X$ dispersion performs a better dispersibility and stability than that of CPM-NiO$_X$ dispersion. Our results provide a powerful evidence for our emulsion process as a good alternative synthesis process.

In general, the film morphology greatly depends on the dispersibility of NPs suspension. We have deposited the NiO$_x$ films on FTO glass from CPM-NiOx and EP-NiOx NPs suspensions, respectively. We have also examined the film morphologies by using AFM and SEM deposited on the FTO glasses. **Figure 3(a)** and **(b)** show the AFM images of the two NiOx films. The FTO glass can be fully covered by CPM-NiO$_X$ and EP-NiO$_X$ films, and also the EP-NiO$_X$ film has a smooth surface morphology with a root-mean square (RMS) roughness equal to 14.73 nm. In comparison to the CPM-NiO$_X$ film with RMS roughness of 20.23 nm, the flat EP-NiOx film may be resulted from the small average NPs size and narrow size distribution of EP-NiOx NPs. In addition, **Figure 3 (c)** and **(d)** shows the top-view oft he SEM images for CPM-NiO$_X$ and EP-NiO$_X$ films. The CPM-NiO$_X$ film exists large aggregates because of the low dispersibility of CPM-NiO$_X$ NPs in DI water. Such large aggregates may affect the formation of perovskite layer on top of the NiO$_X$ film, thereby affecting

the quality of perovskite layer. As for the EP-NiO$_x$ film (**Figure 3(d)**), there is no obvious aggregation on the surface due to the good dispersion of EP-NiOx NPs. Both CPM-NiO$_X$ and EP-NiO$_X$ films coated on FTO glass present high optical transmittance, as shown in their transmission spectra (**Figure S10**). A little lower transmittance of FTO/CPM-NiO$_X$ in the range of 300-500 nm compared to FTO/EP-NiO$_X$ is due to the aggregate induced light scattering.

We evaluate the effect of NiO$_X$ film morphology on the formation of perovskite layer, which perovskite layers were deposited onto the two types of NiO$_X$ films, respectively. From the top-view SEM images of perovskite layers shown in **Figure 4 (a)** and **(b)**, we can see that the morphology of perovskite layer deposited on the CPM-NiO$_X$ layer is not uniform. We further studied the interfacial contact between perovskite and NiO$_X$ using the cross-sectional SEM and elemental mapping of EDS. **Figure 4(c)** presents the cross-sectional SEM image of the perovskite film deposited on CPM-NiO$_X$ layer, showing the poor interfacial contact at the interface of perovskite/CPM-NiO$_X$. The low quality interfacial contact is attributed to the large aggregates presented in CPM-NiO$_X$ film. On the contrary, the good contact can be observed between the perovskite and EP-NiO$_X$ film. (**Figure 4(d)**). As a result, the large aggregates on CPM-NiO$_X$ film affect the formation of perovskite film, resulting in the high trap density in the perovskite film and the poor interfacial contact between perovskite and CPM-NiO$_X$ layer. This kind of film might lead to charge recombination and the FF and V$_{oc}$ losses which result in a poor device performance. **Figure S11** and **S12** show the elemental mapping of cross-sectional EDS of perovskite deposited on EP-NiO$_X$ and CPM-NiO$_X$, respectively. The carbon, NiO$_X$, MAPbI$_3$ and FTO layers were respectively identified by the EDS signal of C-K series, Ni-L series, Pb-M series and Sn-M series.[28] The crystallinity of the perovskite layers is also investigated by XRD measurement, and the XRD patterns of the perovskite layers fabricated on CPM-NiO$_X$ and EP-NiO$_X$ films are shown in Figure 4(e). Both oft he XRD patterns present the characteristic peaks located at 14.29°, 20.13°, 23.67°, 24.62°, 28.64°, 32.08°, 35.24°, 40.88° and 43.36°, which are ascribed to (110), (112), (211), (202), (220), (310), (312), (224) and (314) crystal planes of MAPbI$_3$ tetragonal phase, respectively. There was no significant difference observed in perovskite phase between perovskite films deposited on both NiO$_X$ films. Also, we can conclude that the use of EP-NiO$_X$ NPs can effectively improve the film quality of NiO$_X$ film and also improve the morphology perovskite layer.

11

We fabricated the devices based on the two NiO$_X$ films as the HTL to explore the effect of different NiO$_X$ films on the performance of PVSCs, the device structure and band diagram of each layer of PVSCs is shown in **Figure 5(a)**. The cross-sectional SEM image of the whole device is presented in **Figure 5(b)**, which reveals the thickness of each layer, including EP-NiO$_X$, MAPbI$_3$, PC$_{61}$BM/PEI and Ag with values equal to 40, 375, 60 and 100 nm, respectively. To optimize the process parameters of NiO$_X$ films, we systematically studied the effect of the annealing temperature and the thickness of NiOx on the performance of the devices. **Figure S13** and **Table S2** summarize the performances of PVSCs fabricated from various thickness of EP-NiO$_X$ (20, 40 and 60 nm). The current density decreases from 21.90 to 20.61 mA/cm^2 as the thickness of EP-NiO$_X$ increases. The decreased current density is attributed to the increase of charge transport path, which increases the series resistance. On the other hand, the FF increases from 69.06 to 75.10% as the thickness of EP-NiO$_X$ increases from 20 nm to 60 nm. The improved FF originates from the elimination of pinholes, which can avoid the current leakage. **Figure S14** and **Table S3** summarize the effect of the annealing temperature (without annealing, 100, 150 and 200 ºC) of EP-NiO$_X$ on the device performance. The device fabricated from the EP-NiO$_X$ without annealing and 100 ºC perform the low PCE of 13.11 and 14.82% respectively. Without annealing, the low PCE of these devices is attributed to the residual H$_2$O on the NiO$_X$ films, which affects the formation of perovskite films. With increasing annealing temperature of EP-NiO$_X$ to 150 and 200 ºC, the PCE can be improved to 17.59 and 17.70% respectively, indicating that the PCE of PVSCs fabricated from EP-NiO$_X$ reached a balanced level once the H$_2$O residue was completely removed. Eventually, we have found out that at the temperature of 150 ºC we can get best annealing condition in terms of achieving low temperature and short process time, simultaneously. As a result, the EP-NiO$_X$ with 40 nm thickness and the annealing temperature of 150 ºC was used throughout this study. The J-V curves and photovoltaic characteristics of the PVSCs fabricated from CPM-NiO$_X$ and EP-NiO$_X$ are shown in **Figure 5(c)** and summarized in **Table 1**. The champion device with active area of 0.09 cm^2 fabricated from EP-NiO$_X$ can reach PCE equal to 18.85% with the V$_{oc}$ of 1.08 V, the J$_{sc}$ of 21.47 mA/cm^2, and the fill factor (FF) of 81.34%. PCE is much higher comparing to the devices fabricated from CPM-NiO$_X$ (16.68%). **Figure 5(d)** shows the Maximum Power Point Tracking (MPPT) measurement for the PVSCs fabricated with EP-NiO$_X$, presenting the stabilized current density of 20.2 mA/cm^2 (J$_{MPP}$) and PCE of 18.1% obtained while holding at maximum power voltage equal to 0.9 V for

100 s. **Figure 5(e)** shows the External Quantum Efficiency (EQE) measurement of the devices with two HTLs. The device with EP-NiO$_X$ exhibits improved EQE from 400 to 800 nm. The integrated current densities from the EQE spectra for the PVSCs using EP-NiO$_X$ and CPM-NiO$_X$ are 20.56 and 19.07 mA/cm^2, respectively, which is consistent with the J$_{sc}$ obtained from J-V measurement. These results certificate the accuracy of J-V measurements. We fabricated the larger area (1 cm^2) devices based on EP-NiOx and CPM-NiOx, respectively, and the performance are shown in **Figure S15**. When the device area is increased from 0.09 to 1 cm^2, the PCEs of the devices fabricated from EP-NiOx and CPM-NiOx are 13.93% and 10.06%, respectively. According to our previous studies,[28] the PCE reduction of the large-area devices is mainly due to the larger resistance of transparent electrode (FTO). The PCE reduction can be greatly improved by increasing the conductivity of the FTO, but this subject is beyond the scope of this study. In addition, a large-scale morphology of different places of the perovskite films has been provided for proving the non-uniform perovskite layer deposited on CPM-NiO$_X$ film, as shown in **Figure S16**. The PCE reduction of CPM-NiOx based devices (~40%) is greater than that of EP-NiOx based devices (~26%). This result shows that the uniformity of HTL has a more significant impact on the PCE of large-area devices and proves that the EP-NiOx film is more suitable for future large-area mass-production process. Increasing PCE of PVSCs with EP-NiO$_X$ mainly results from the improvements of V$_{oc}$, J$_{sc}$ and FF, which can be attributed to the improvement of morphology of NiO$_X$ film and interfacial properties at HTL/perovskite interface. The J–V characteristics of the PVSCs fabricated using CPM-NiO$_X$ and EP-NiO$_X$ in the forward and reverse scanning directions were measured. Both devices present a negligible hysteresis behavior (**Figure S17**). Furthermore, we have evaluated the uniformity of different batches of NiO$_X$ NPs by investigating the particle size and manufacturing PVSCs using different batches of NiO$_X$ NPs. The particle size of different batches of EP-NiO$_X$ NPs and CPM-NiO$_X$ NPs are shown in **Table S4**. The EP-NiO$_X$ NPs show excellent uniformity from batch-to-batch with the average particle size around 8 nm and small standard deviation. In contrast, the CPM-NiO$_X$ NPs present larger particle size, higher standard deviation and lower batch-to-batch uniformity. Moreover, the performance of PVSCs fabricated from EP-NiO$_X$ films exhibit a good batch-to-batch uniformity, indicating the consistent quality of different batches of EP-NiO$_X$ NPs. However, the PCE of PVSCs fabricated from different batches of CPM-NiO$_X$ NPs varies from batch to batch, as shown in **Figure S18**. The results from the particle size and

13

devices performance indicates that it is not easy to control the quality of NiO_X NPs in different batches by using chemical precipitation method. Furthermore, we have demonstrated the stability of PVSCs fabricated from different HTLs, see **Figure 5(f)**. All the devices have been encapsulated with UV curable resin and dark stored at ambient condition (25ºC and 40%~60% RH). Thus we can ensure that the stability test is not influenced by moisture and heat. The device lifetime was obtained by doing dark measurements periodically. The PCE of PVSCs fabricated from CPM-NiOx film decayed to 80% of its initial value in about 30 days, however, the PCE of PVSCs fabricated from EP-NiOx film remained at its initial level. Even though the devices have been encapsulated, the intrinsic deterioration of PVSCs fabricated from CPM-NiO_X film is still significant. This result may be due to the defects caused by a poor morphology of the perovskite film, and the defects would accelerate the degradation of the PVSCs. Finally, we demonstrate the potential of EP-NiO_X for flexible optoelectronics. We fabricated the flexible PVSCs based on flexible substrate (mica/AZO-ITO) with PCE of 14.28% (V_{oc}:1.03 V, J_{sc}: 20.56 mA/cm^2 and FF: 68.19%), as shown in **Figure S19**. These results show that the new NiO_X NP synthesis method presented in our research is greatly beneficial for the commercialization of perovskite solar cells.

To further clarify the factors of how the EP-NiO_X HTL improves the device performance, we have conducted a detailed analysis of the trap-assisted recombination processes of PVSCs fabricated using these two HTLs. To investigate the trap-density, the space charge limited current (SCLC) model with the equation $V_{TFL}= eN_td^2/(2\varepsilon\varepsilon_0)$ was conducted, where V_{TFL} represents the trap-filled limited (TFL) voltage, e represents the elementary charge, ε and ε_0 are the dielectric constant of perovskite and the permittivity of free space, N_t is the trap defect density, and d is the thickness of perovskite film. **Figure 6(a)** shows the I-V curve of the hole-only devices with structure of FTO/HTL/perovskite/Au. The V_{TFL} is determined by transition point between Ohmic region and TFL region, so the trap-density (N_t) of perovskite fabricated on CPM-NiO_X and EP-NiO_X can be obtained with the values equal to 3.88×10^{16} and 1.80×10^{16} cm^{-3}, respectively. Further, the drift-diffusion model has been applied to simulate PVSCs. The experimental and simulation I-V curves under different light intensities are shown in **Figure S20 and S21**. Also, more detailed description of the model can be found in the reference **[Nano Energy 67 (2020) 104186]**. The fitted parameters used in the modeling are shown in **Table 2**. **Figure 6(b)** shows the results of FF and V_{oc} under different light intensities. The simulations

present a very good agreement with the experimental results for both types of NiO_x samples. The bulk defect densities ($N_{t,bulk}$) are equal to 2.09×10^{16} and 0.94×10^{16} cm^{-3} for CPM-NiO_x and EP-NiO_x samples, respectively. This stays in a good agreement with the SCLC results. It has been also found that the interfaces have much worse quality for CPM-NiO_x with the trap defect density ($N_{t,inter}$) equals to 1.37×10^{12} cm^{-2} if compared to EP-NiO_x with defect density equal to only 1.02×10^{9} cm^{-2}. It could be also noticed that the shunt resistance is much more pronounced in CPM-NiO_x (0.61×10^{4} Ω cm^{2}) than in EP-NiO_x (4.38×10^{4} Ω cm^{2}). Consequently, we can conclude that the perovskite film fabricated on EP-NiO_X film exhibits less trapped states in the bulk and at the interfaces due to the better quality and better contact as compared to that on CPM-NiO_X film. To understand the effect of trap-density on the characteristics of charge recombination process, the relationship between the V_{oc} and the light intensity was used to explore the recombination mechanism. In general, the light intensity dependence of the V_{oc} reveals the recombination mechanism in solar cell, and the recombination behavior can be divided into bimolecular and trap-assisted recombination process. According to the previous reports,[29] if the slope of V_{oc} versus light intensity close to kT/q, where q is the electron charge, k is the Boltzmann constant, and T is the Kelvin temperature, the recombination process is dominated by bimolecular process. While the slope is greater than kT/q, the recombination behavior will tend to be trap-assisted recombination. In **Figure 6(b)**, we can find that slope of the PVSCs fabricated from EP-NiO_X is 1.704 kT/q, which is much lower than that of PVSCs fabricated from CPM-NiO_X film (2.307 kT/q). This result indicates that the trap-assisted charge recombination in PVSCs fabricated from EP-NiO_X film is significantly suppressed due to the reduction of trap-states in the perovskite layer. The shunt resistance that is lower for CPM-NiO_x is explained with the aggregation of NiO_x structure that led to higher chance of shunting the sample, see **Figure 4(c)**. We have further investigated the charge separation behavior for PVSCs with different HTLs by using the steady state photoluminescence (PL) and the PL spectrum are shown in **Figure 6(c)**. When we deposited the perovskite films on the CPM-NiO_X and EP-NiO_X respectively, we observed a significant PL quenching for EP-NiO_X/$MAPbI_3$ film because of the efficient hole extraction. Furthermore, TRPL measurements were also performed as illustrated in **Figure 6(d)**. The exponential decay profiles were fitted by the bi-exponential decay model as follow : $I(t) = A_1 \exp(-t/\tau_1) + A_2 \exp(-t/\tau_2)$, where A_1 represents the fraction of charge transfer from perovskite to HTL, τ_1 represents the charge transfer lifetime, A_2 represents the fraction of charge

recombination, and τ_2 is the charge recombination lifetime in perovskite layer. The average lifetime was calculated by following equation: $\tau_{avg} = \sum_i A_i \tau_i / \sum_i A_i$. The calculated τ_{avg} of perovskite films fabricated on CPM-NiO$_X$ and EP-NiO$_X$ films are 18.9 and 9.2 ns, respectively, indicating that the EP-NiO$_X$ film exhibits more efficient hole extraction ability than that of CPM-NiO$_X$. The efficient charge extraction ability can accelerate the charge transfer and suppress the non-radiative recombination, and thus improve the device performance. These improvements can be attributed to the good interfacial properties at the EP-NiO$_X$/perovskite interface, which is originated from the excellent dispersibility of EP-NiO$_X$ NPs.

4. Conclusion

In this study, we have reported an emulsion process, which can control the size and uniformity of nanoparticles, to synthesize NiOx NPs with high reproducibility. The emulsion process used a novel surfactant tetramethylammonium hydroxide (TMAOH) that can form micelles as nano-reactors containing hydroxide anion. In contact with nickel nitrate aqueous solution, the Ni(OH)$_2$ NPs were formed in the nano-reactor with controlled size and distribution. The NiO$_X$ NPs were then obtained by calcining the Ni(OH)$_2$ NPs at 270 °C for 2 h. The NiO$_X$ NPs with the size of 8.28±2.64 nm can be easily dispersed in water without any aggregation and form stable solution. The smooth and uniform NiO$_X$ HTL film can be obtained by solution process. A uniform and smooth perovskite film can thus be fabricated on the top of this smooth HTL. As a result, the PVSCs fabricated from EP-NiO$_X$ can perform the high PCE of 18.85%, which is higher than that of CPM-NiO$_X$ of 16.68%. The flexible PVSCs fabricated from EP-NiO$_X$ were also demonstrated with the PCE of 14.3%. Except for the improvement of performance, the quality of EP-NiO$_X$ NPs shows a good batch-to-batch uniformity, resulting in the highly reproducible HTL film and PVSCs. The EP-NiO$_X$ NPs developed in this work could be a potential HTL to be used in the fabrication of highly efficient PVSCs by solution process at low temperature. This make the large-scale process feasible at low cost and low energy consumption.

Declaration of Competing Interest

There are no conflicts to declare.

Acknowledgements

Reference

[1] National Renewable Energy Laboratory. Best Research-Cell Efficiencies. 2019. Available at http://www.nrel.gov/pv/assets/images/efficiency_chart.jpg.

[2] M. Kim, G.-H. Kim, T. K. Lee, I. W. Choi, H. W. Choi, Y. Jo, Y. J. Yoon, J. W. Kim, J. Lee, D. Huh, H. Lee, S. K. Kwak, J. Y. Kim, D. S. Kim, Methylammonium chloride induces intermediate phase stabilization for efficient perovskite solar cells, Joule 3 (2019) 2179-2192.

[3] Q. Jiang, Y. Zhao, X. Zhang, X. Yang, Y. Chen, Z. Chu, Q. Ye, X. Li, Z. Yin, J. You, Surface passivation of perovskite film for efficient solar cells, Nat. Photonics. 13 (2019) 460-466.

[4] M. Saliba, J.-P. Correa-Baena, C. M. Wolff, M. Stolterfoht, N. Phung, S. Albrecht, D. Neher, A. Abate, How to make over 20% efficient perovskite solar cells in regular (n–i–p) and inverted (p–i–n) architectures, Chem. Mater. 30 (2018) 4193-4201.

[5] X. Zheng, Y. Hou, C. Bao, J. Yin, F. Yuan, Z. Huang, K. Song, J. Liu, J. Troughton, N. Gasparini, C. Zhou, Y. Lin, D.-J. Xue, B. Chen, A. K. Johnston, N. Wei, M. N. Hedhili, M. Wei, A. Y. Alsalloum, P. Maity, B. Turedi, C. Yang, D. Baran, T. D. Anthopoulos, Y. Han, Z.-H. Lu, O. F. Mohammed, F. Gao, E. H. Sargent, O. M. Bakr, Managing grains and interfaces via ligand anchoring enables 22.3% efficiency inverted perovskite solar cells, Nat. Energy. 5 (2020) 131-140.

[6] H. Elbohy, B. Bahrami, S. Mabrouk, K. M. Reza, A. Gurung, R. Pathak, M. Liang, Q. Qiao, K. Zhu Adv. Funct. Mater. Tuning hole transport layer using urea for high-performance perovskite solar cells, 29 (2018) 1806740.

[7] K. Jiang, F. Wu, G. Zhang, P. C. Y. Chow, C. Ma, S. Li, K. S. Wong, L. Zhu, H. Yan, Inverted planar perovskite solar cells based on CsI-doped PEDOT:PSS with efficiency beyond 20% and small energy loss, J. Mater. Chem. A. 7 (2019) 21662-21667.

[8] S. Yang, S. Chen, E. Mosconi, Y. Fang, X. Xiao, C. Wang, Y. Zhou, Z. Yu, J. Zhao, Y. Gao, F. De Angelis,

J. Huang, Stabilizing halide perovskite surfaces for solar cell operation with wide-bandgap lead oxysalts, Science 365 (2019) 473.

[9] H. Wang, Z. Yu, J. Lai, X. Song, X. Yang, A. Hagfeldt, L. Sun, One plus one greater than two: high-performance inverted planar perovskite solar cells based on a composite CuI/CuSCN hole-transporting layer, J. Mater. Chem. A. 6 (2018) 21435-21444.

[10] C. Zuo, L. Ding, Solution-processed Cu_2O and CuO as hole transport materials for efficient perovskite solar cells, Small 11 (2015) 5528-5532.

[11] P.-H. Lee, B.-T. Li, C.-F. Lee, Z.-H. Huang, Y.-C. Huang, W.-F. Su, High-efficiency perovskite solar cell using cobalt doped nickel oxide hole transport layer fabricated by NIR process, Sol. Energy Mater Sol. Cells. 208 (2020) 110352.

[12] X. Yin, J. Zhai, P. Du, N. Li, L. Song, J. Xiong, F. Ko, 3 D NiO Nanowall hole-transporting layer for the passivation of interfacial contact in inverted perovskite solar cells ChemSusChem. 13 (2020) 1006–1012.

[13] J. Y. Jeng, K. C. Chen, T. Y. Chiang, P. Y. Lin, T. D. Tsai, Y. C. Chang, T. F. Guo, P. Chen, T. C. Wen, Y. J. Hsu, Nickel oxide electrode interlayer in $CH_3NH_3PbI_3$ perovskite/PCBM planar-heterojunction hybrid solar cells, Adv. Mater. 26 (2014) 4107-4113.

[14] Z. Liu, J. Chang, Z. Lin, L. Zhou, Z. Yang, D. Chen, C. Zhang, S. F. Liu, Y. Hao, High-performance planar perovskite solar cells using low temperature, solution–combustion-based nickel oxide hole transporting layer with efficiency exceeding 20%, Adv. Energy Mater. 8 (2018) 1703432.

[15] X. Yin, Y. Guo, H. Xie, W. Que, L. B. Kong, Nickel oxide as efficient hole transport materials for perovskite solar cells, Solar RRL. 3 (2019) 1900001.

[16] X. Zheng, Z. Song, Z. Chen, S. S. Bista, P. Gui, N. Shrestha, C. Chen, C. Li, X. Yin, R. A. Awni, H. Lei, C. Tao, R. J. Ellingson, Y. Yan, G. Fang, Interface modification of sputtered NiOx as the hole-transporting layer for efficient inverted planar perovskite solar cells, J. Mater. Chem. C. 8 (2020) 1972-1980.

[17] J. Cui, F. Meng, H. Zhang, K. Cao, H. Yuan, Y. Cheng, F. Huang, M. Wang, $CH_3NH_3PbI_3$-based planar solar cells with magnetron-sputtered nickel oxide, ACS Appl. Mater. Interfaces. 6 (2014) 22862-22870.

[18] G. Li, Y. Jiang, S. Deng, A. Tam, P. Xu, M. Wong, H. S. Kwok, Overcoming the limitations of sputtered nickel oxide for high-efficiency and large-area perovskite solar cells, Adv. Sci. 4 (2017) 1700463.

[19] S. Seo, I. J. Park, M. Kim, S. Lee, C. Bae, H. S. Jung, N. G. Park, J. Y. Kim, H. Shin, An ultra-thin, un-doped NiO hole transporting layer of highly efficient (16.4%) organic–inorganic hybrid perovskite solar cells, Nanoscale 8 (2016) 11403-11412.

[20] X. Yin, M. Que, Y. Xing, W. Que, High efficiency hysteresis-less inverted planar heterojunction perovskite solar cells with a solution-derived NiOx hole contact layer, J. Mater. Chem. A. 3 (2015) 24495-24503.

[21] L. J. Tang, X. Chen, T. Y. Wen, S. Yang, J. J. Zhao, H. W. Qiao, Y. Hou, H. G. Yang, A solution-processed transparent NiO hole-extraction layer for high-performance inverted perovskite solar cells, Chem. Eur. J. 24 (2018) 2845-2849.

[22] X. Liang, Q. Yi, S. Bai, X. Dai, X. Wang, Z. Ye, F. Gao, F. Zhang, B. Sun, Y. Jin, Synthesis of unstable colloidal inorganic nanocrystals through the introduction of a protecting ligand, Nano Lett. 14 (2014) 3117-3123.

[23] Z. Liu, A. Zhu, F. Cai, L. Tao, Y. Zhou, Z. Zhao, Q. Chen, Y.-B. Cheng, H. Zhou, Nickel oxide

nanoparticles for efficient hole transport in p-i-n and n-i-p perovskite solar cells, J. Mater. Chem. A. 5 (2017) 6597-6605.

[24] X. Yin, P. Chen, M. Que, Y. Xing, W. Que, C. Niu, J. Shao, Highly efficient flexible perovskite solar cells using solution-derived NiOx hole contacts, ACS Nano. 10 (2016) 3630-3636.

[25] H. Zhang, J. Cheng, F. Lin, H. He, J. Mao, K. S. Wong, A. K. Jen, W. C. Choy, Pinhole-free and surface-nanostructured NiOx film by room-temperature solution process for high-performance flexible perovskite solar cells with good stability and reproducibility, ACS Nano. 10 (2016) 1503-1511.

[26] L. Bronstein, M. Antonietti, P. Valetsky, Metal colloids in block copolymer micelles: Formation and material properties, In Nanoparticles and Nanostructured Films, pp 145-171.

[27] M.-H. Jao, C.-C. Cheng, C.-F. Lu, K.-C. Hsiao, W.-F. Su, Low temperature and rapid formation of high quality metal oxide thin film via a hydroxide-assisted energy conservation strategy, J. Mater. Chem. C. 6 (2018) 9941-9949.

[28] Y.-C. Huang, F.-H. Hsu, H.-C. Cha, C.-M. Chuang, C.-S. Tsao, C.-Y. Chen, High-performance ITO-free spray-processed polymer solar cells with incorporating ink-jet printed grid, Org. Electron. 14 (2013) 2809–2817

[29] D. Głowienka, D. Zhang, F. Di Giacomo, M. Najafi, S. Veenstra, J. Szmytkowski, Y. Galagan, Role of surface recombination in perovskite solar cells at the interface of HTL/$CH_3NH_3PbI_3$ Nano Energy. 67 (2020) 104186.
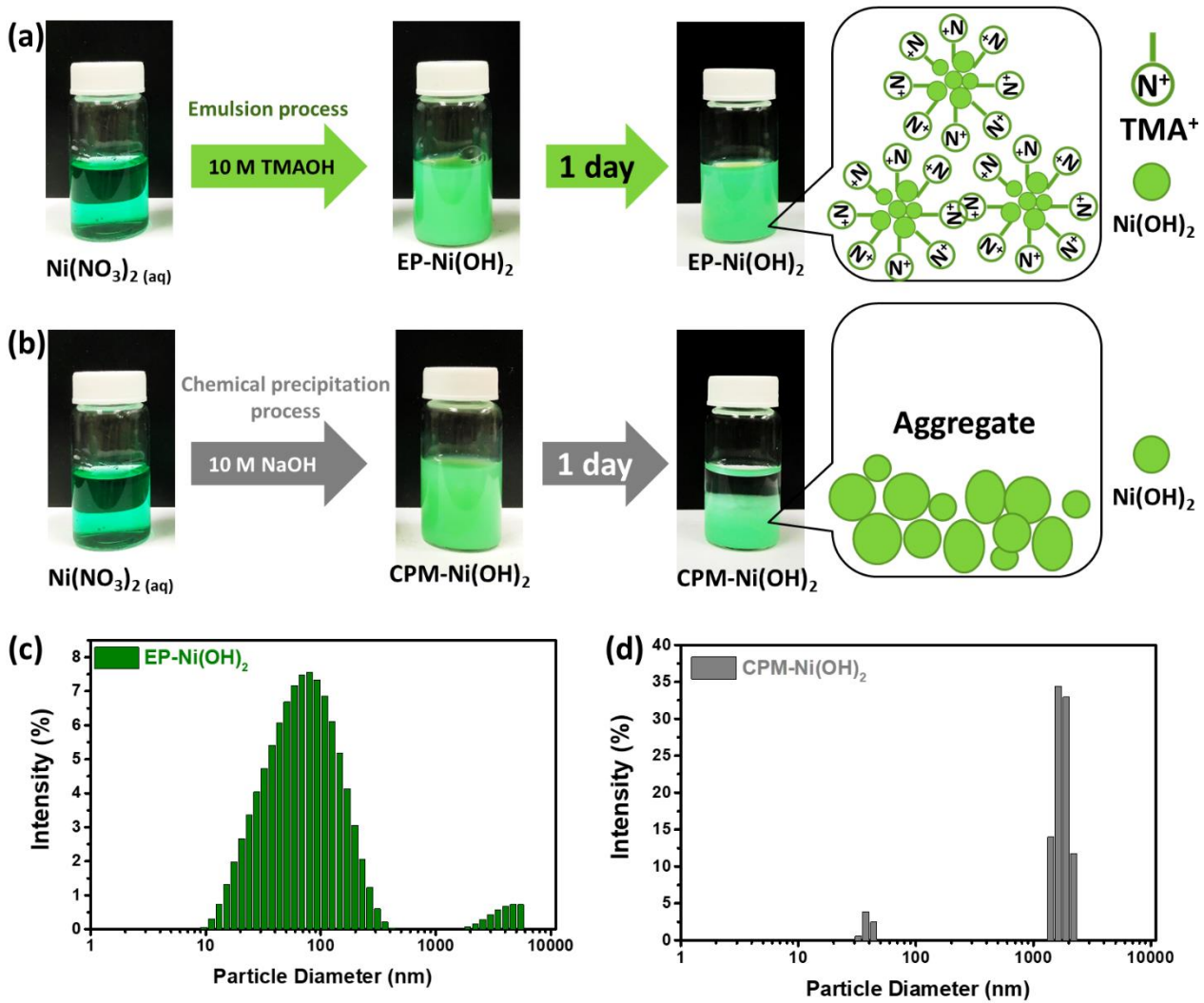
Figure 1. Schematic diagrams of Ni(OH)$_2$ nanoparticles synthesized by (a) emulsion process and (b) chemical precipitation method. DLS measurement of (c) EP-Ni(OH)$_2$ NPs and (d) CPM-Ni(OH)$_2$ NPs aqueous solution.
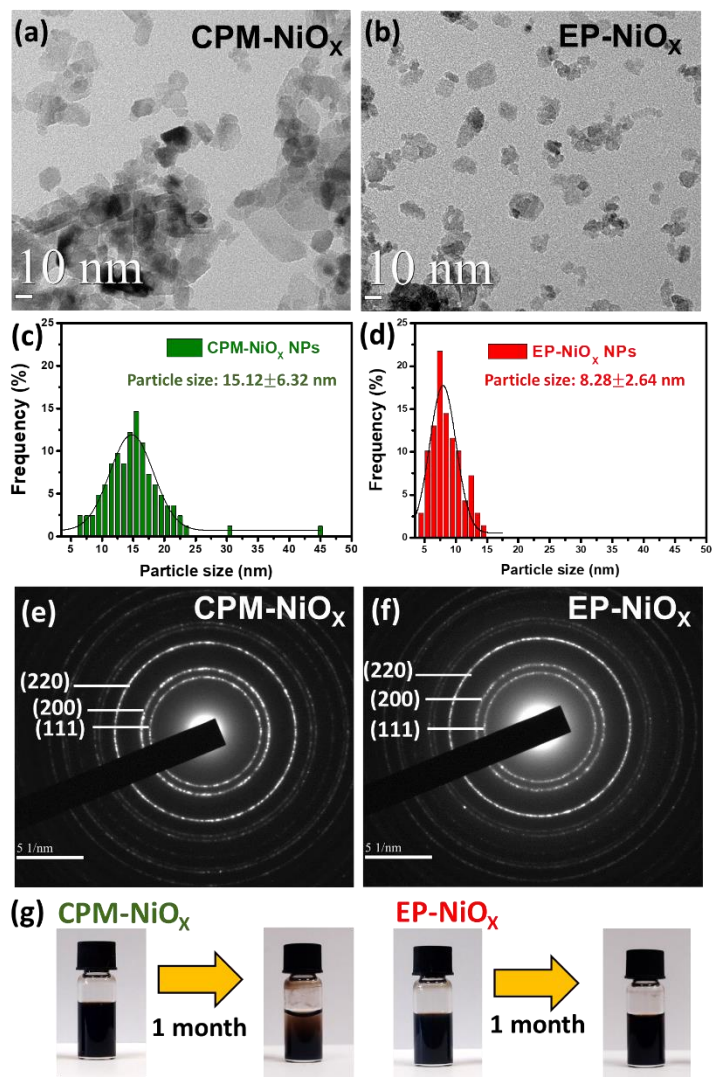
Figure 2. (a-b) TEM images, **(c-d)** particles size distribution (estimated from TEM image) and **(e-f)** SAED patterns of CPM-NiO$_X$ and EP-NiO$_X$ NPs. (g) Stability photo of CPM-NiO$_X$ NPs (left) and EP-NiO$_X$ NPs (right) suspension after one month storage.
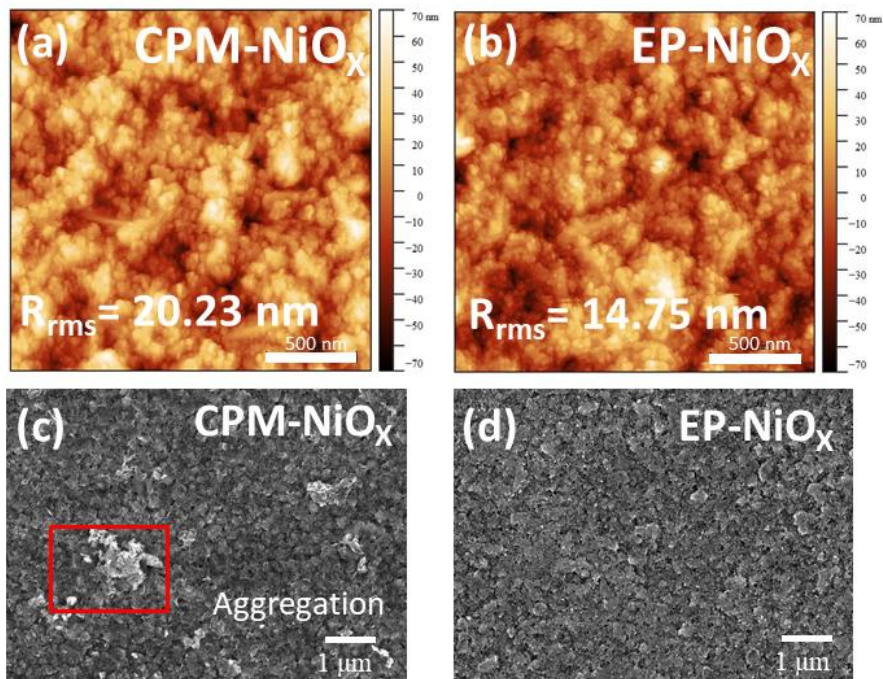
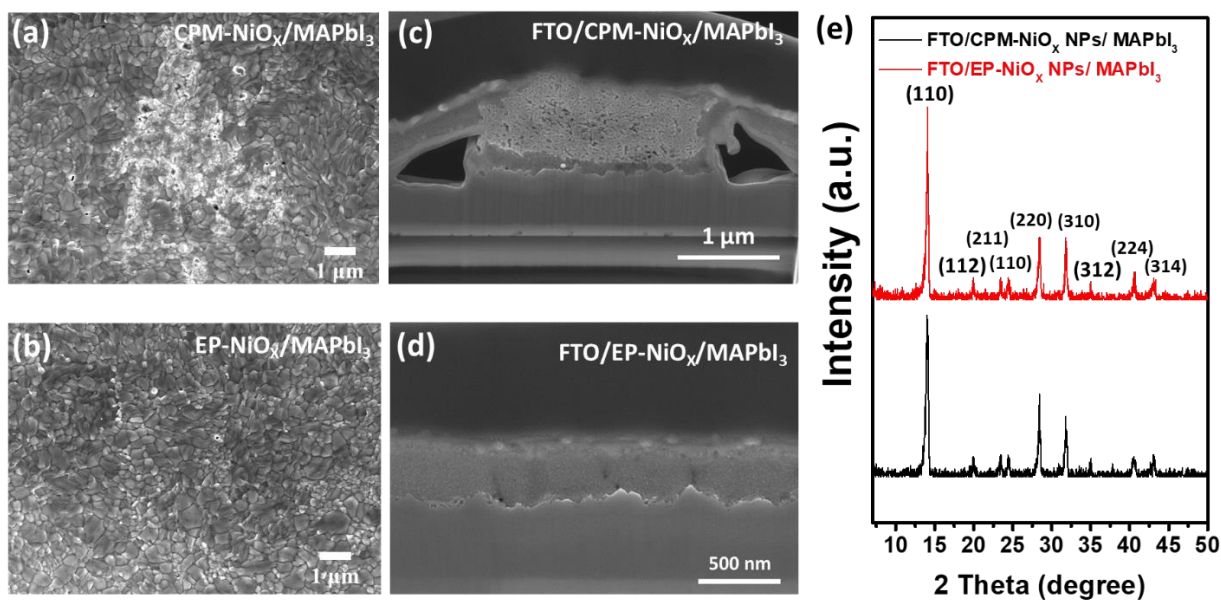**Figure 3.** AFM and SEM images of (a-b) CPM-NiO$_X$ and (c-d) EP-NiO$_X$ film deposited on FTO glass.

Figure 4. Top-view and cross-sectional SEM images of perovskite films deposited on (a,c) CPM-NiO$_X$ and (b,d) EP-NiO$_X$ film. (e) XRD pattern of perovskite films deposited on films of CPM-NiO$_X$ and EP-NiO$_X$ respectively.
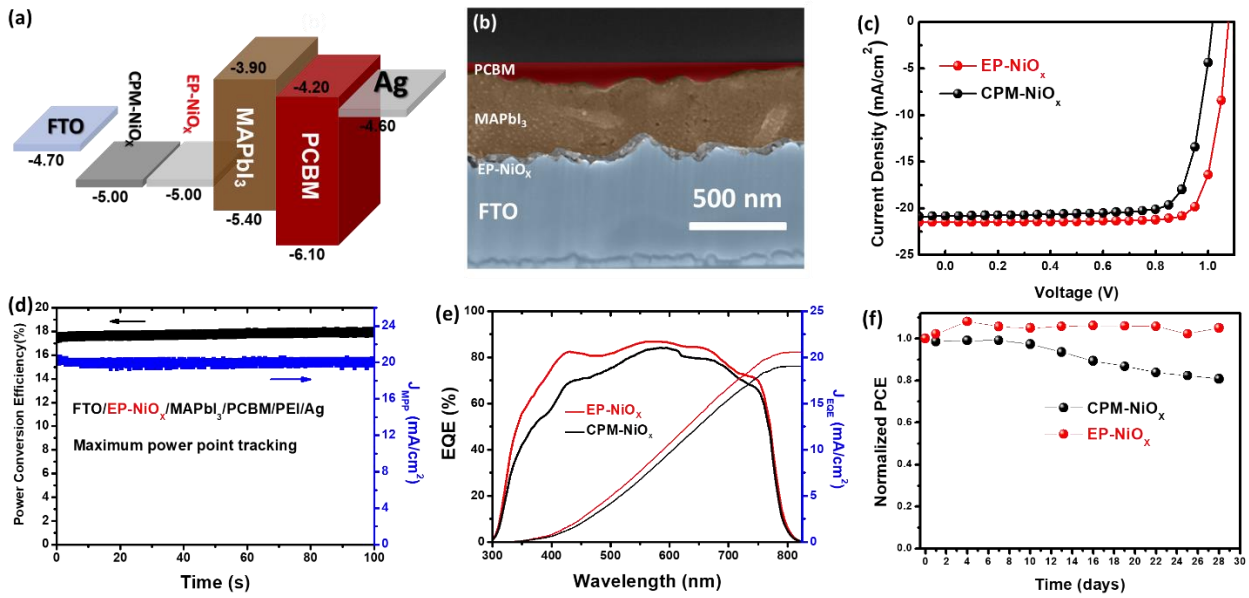
Figure 5. (a) Energy level diagram (relative to vacuum) of each material in PVSCs. (b) Cross-section image of PVSCs fabricated from EP-NiO$_X$ film. (c) Devices performance, (d) MPPT, (e) EQE measurements and (f) stability of PVSCs fabricated from CPM- NiO$_X$ and EP-NiO$_X$ films.
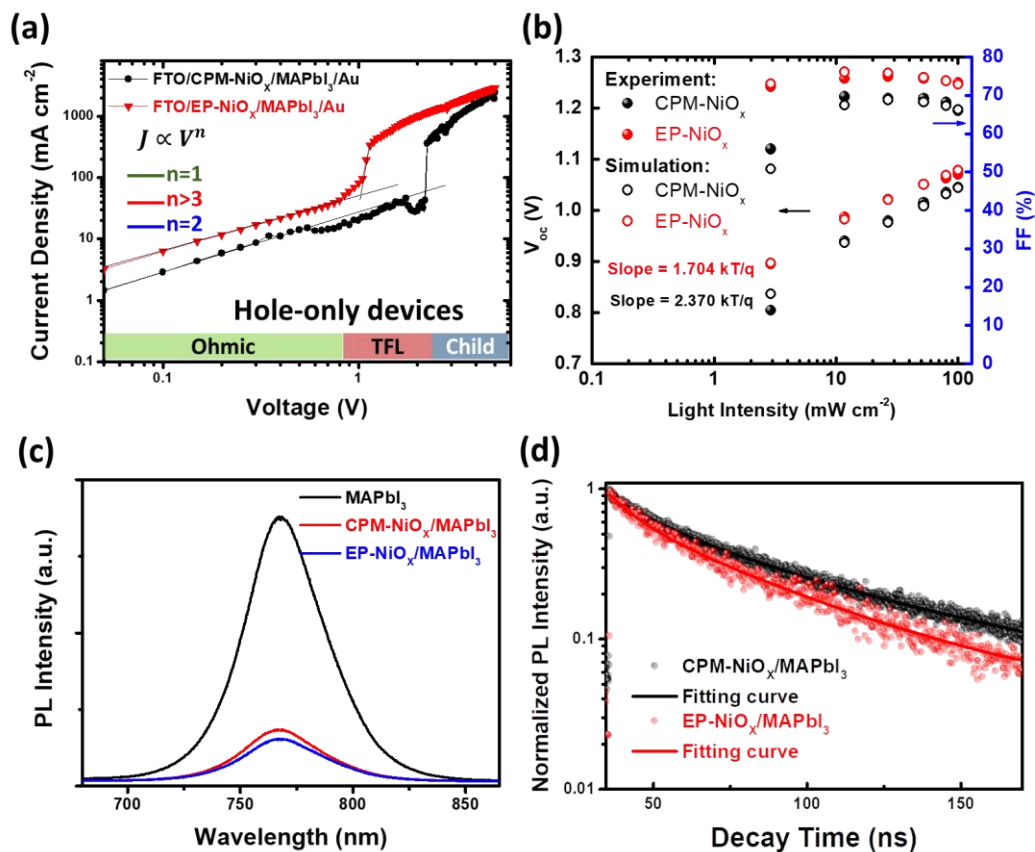
Figure 6. (a) SCLC measurement of hole-only device and (b) photovoltaic parameters of V_{oc}, and FF measured under different light intensities for PVSCs fabricated from CPM-NiO$_X$ and EP-NiOx films. (c) Steady-state PL and (d) TRPL spectrum of perovskite films deposited on CPM-NiO$_X$ and EP-NiO$_X$ film.

Table 1. Device characteristics of p-i-n PVSCs fabricated from CPM-NiO$_X$ and EP-NiO$_X$.

Sample	V_{oc} (V)	J_{sc} (mA/cm^2)	FF (%)	PCE[a] (%)
EP-NiO$_x$	1.08 (1.08 ±0.02)	21.47 (21.14 ±0.21)	81.34 (78.97 ±2.12)	18.85 (17.95 ±0.55)
CPM-NiO$_x$	1.02 (1.03 ±0.02)	20.81 (19.76 ±1.05)	78.81 (74.54 ±2.89)	16.68 (15.21 ±0.85)

[a] The average data are obtained at least 12 devices in the bracket.

Table 2. Parameters used in the drift-diffusion simulations of PSCs with EP and CPM NiO$_x$

Model	Parameter	Unit	CPM-NiO$_X$	EP-NiO$_X$
SCLC	Bulk trap density ($N_{t,bulk}$)	cm^{-3}	3.88×10^{16}	1.80×10^{16}
Drift-diffusion	Bulk trap density ($N_{t,bulk}$)	cm^{-3}	2.09×10^{16}	0.94×10^{16}
	Interface trap density ($N_{t,inter}$)	cm^{-2}	1.37×10^{12}	1.02×10^{9}
	Shunt resistance (R_{sh})	Ω cm^2	0.61×10^4	4.38×10^4